Acta Crystallographica Section B
Structural Science
ISSN 0108-7681

Calcium–lead fluoro-vanadinite apatites. I. Disequilibrium structures

ZhiLi Dong* and T. J. White

Centre for Advanced Research of Ecomaterials, Institute of Environmental Science and Engineering, Innovation Centre, Nanyang Technological University, Block 2, Unit 237, 18 Nanyang Drive, Singapore 637723, Singapore

Correspondence e-mail: zldong@ntu.edu.sg

Received 27 November 2003
Accepted 24 January 2004

The synthetic vanadinites $(Pb_xCa_{10-x})(VO_4)_6F_{2\delta}$, $1 < x < 9$, adopt a $P6_3/m$ apatite structure with $9.7590\,(1) \leq a \leq 10.1179\,(1)$ Å and $7.0434\,(3) \leq c \leq 7.4021\,(1)$ Å. The partitioning of calcium and lead over the $A^{\rm I}(4f)$ and $A^{\rm II}(6h)$ positions is nonstoichiometric with lead preferentially entering the larger $A^{\rm II}$ site. High-resolution electron microscopy showed that samples annealed for 10 h at 1073 K are in disequilibrium with calcium- and lead-rich microdomains coexisting at unit-cell scales. For $(Pb_5Ca_5)(VO_4)_6F_{2\delta}$, sintering in excess of 2 weeks is required for the metals to order macroscopically. As annealing progresses, c/a, the partitioning coefficient $k_{\rm Pb}(A^{\rm I}/A^{\rm II})$ and the $A^{\rm I}O_6$ metaprism twist angle (φ) adjust cooperatively to enlarge the apatite channel, and thereby accommodate higher lead content. These results demonstrate that φ is a sensitive measure of disequilibrium and a useful device for monitoring changes in apatite topology as a function of composition.

1. Introduction

The apatite family is most often described by the general formula $[A^{\rm I}_4][A^{\rm II}_6]B{\rm O}_4)_6X_2$, although $[A_{10}](B{\rm O}_5)_6X_2$ and $[A_{10}](B{\rm O}_3)_6X_2$ derivatives are observed less commonly (White & Dong, 2003). All belong to maximal non-isomorphic subgroups of $P6_3/mcm$ (193). In $P6_3/m$ apatites the $A^{\rm I}$ and $A^{\rm II}$ cation acceptor sites accommodate large mono-, di- and trivalent ions, while B positions are filled by smaller 3^+, 4^+, 5^+, 6^+ and 7^+ metals and metalloids. The X anion site, which may be highly nonstoichiometric, is normally occupied by halides, oxygen or hydroxyl, and rarely by boron, copper or cyanamide (Ito *et al.*, 1988; Carrillo-Cabrera & von Schnering, 1999; Habelitz *et al.*, 1999). Apatites can be derived from regular anion nets and deviations from this ideal proves useful for systematizing composition and structure. In particular, the $A^{\rm I}O_6$ metaprism twist angle (φ) is a sensitive measure of A-cation ordering (White *et al.*, 2004).

Apatite and several related minerals hold considerable promise for the stabilization and recycling of industrial waste and are already applied to the treatment of lead-contaminated soils and waters (Jeanjean *et al.*, 1994; Zhang & Ryan, 1999; Ioannidis & Zouboulis, 2003). However, the apatites are a diverse group and systematic crystal chemistry studies for simplified (non-phosphate) systems relevant to waste immobilization remain sparse. Apatite-group minerals with potential environmental technology applications include the prototype $Ca_{10}(PO_4)_6(F,Cl,OH)_2$ (Kim *et al.*, 2000), pyromorphite $Pb_{10}(PO_4)_6Cl_2$ (Dai & Hughes, 1989), mimetite

Table 1
Refined cell parameters and k_{Pb} for $(Pb_xCa_{10-x})(VO_4)_6(F_{1-2y}O_y\square_y)_2$ annealed for 10 h at 1073 K.

x = 0: $Ca_{10}(VO_4)_6F_2$ is strictly monoclinic, space group $P2_1/m$, with a = 9.711 (2), b = 9.708 (2), c = 7.0159 (3) Å; γ = 120.02 (2)°; V = 572.6 (2) Å^3.

x	0	1	2	3	4	5	6	7	8	9
a (Å)	9.7073 (4)	9.7590 (1)	9.8125 (1)	9.8534 (1)	9.9027 (1)	9.9462 (1)	9.9980 (1)	10.0372 (1)	10.0762 (1)	10.1179 (1)
c (Å)	7.0153 (3)	7.0434 (1)	7.0779 (1)	7.1084 (1)	7.1455 (1)	7.1983 (1)	7.2502 (1)	7.3039 (1)	7.3585 (1)	7.4021 (1)
V (Å^3)	572.5 (5)	581.0 (1)	590.2 (2)	597.7 (2)	606.8 (2)	616.7 (2)	627.6 (1)	637.2 (2)	647.0 (2)	656.2 (2)
N(Ca1)†	1	0.93 (3)	0.83 (4)	0.77 (5)	0.71 (6)	0.61 (6)	0.55 (6)	0.52 (7)	0.37 (8)	0.20 (8)
N(Ca2)	1	0.91 (3)	0.76 (3)	0.70 (4)	0.62 (6)	0.49 (6)	0.31 (7)	0.22 (8)	0.18 (10)	0.13 (8)
$k_{Pb}(A^I/A^{II})$‡		0.54	0.47	0.51	0.51	0.52	0.43	0.41	0.51	0.61

† $N(A^I) = N$(Ca1) + N(Pb1) = 1 and $N(A^{II}) = N$(Ca2) + N(Pb2) = 1. ‡ $k_{Pb}(A^I/A^{II}) = [2 - 2N(Ca1)]/[3 - 3N(Ca2)]$. For equal partitioning of Pb over A^I and A^{II}, K_{Pb} would be 0.66 for all compositions.

$Pb_{10}(AsO_4)_6Cl_2$ (Calos & Kennard, 1990) and vanadinite $Pb_{10}(VO_4)_6Cl_2$ (Dai & Hughes, 1989).

Because eco-apatites encompass a wide range of compositions, a holistic crystallochemical account of the systematic changes that occur as a function of composition and processing conditions is required. One approach is that of Elliott (1973), where the rather regular ...*ABA*... hexagonal close-packing arrangement of BO_4 tetrahedra is emphasized with the interstices occupied to produce columns of larger A cations and X anions. On this basis, simple trigonometry allows the predication that the a axis will dilate more rapidly than the c axis as larger ions are inserted. In a related, but different simplification, Dong & White (2004) considered the regular triangular network of oxygen as the key tessellation that through rotation could generate a range of distorted structures in response to variations in the average ionic radius of the cell contents. In this description the fundamental parameter was defined as the A^IO_6 metaprism twist angle (Fig. 1) that adopts values from 0 to 60° in response to changes in chemistry. Like the description of Elliott, this method rationalized the relative changes in cell parameters and additionally emphasized the one-dimensional tunnels and adaptable framework nature of apatites.

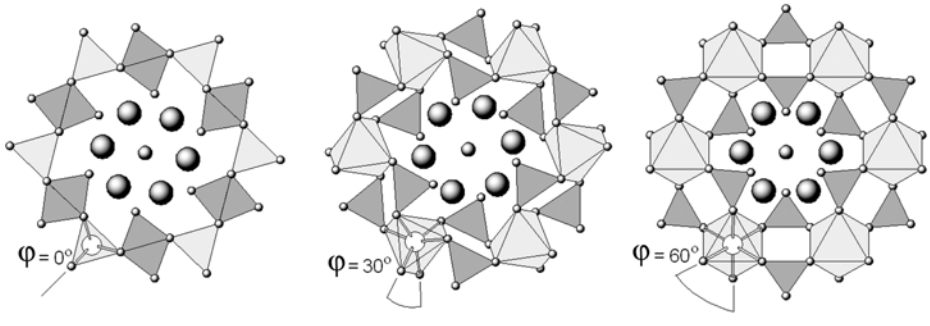

Figure 1
Polyhedral representations of idealized $[A^I_4][A^{II}_6](BO_4)_6X_2$ apatites emphasizing the A^IO_6 trigonal prisms/metaprisms (light shading) and BO_4 tetrahedra (dark shading). In this depiction [0001] channels are evident as the locations of A^{II} cations and X anions. To accommodate a necessary shortening of bond lengths as the relative crystal radii of channel atoms decrease, the A^IO_6 units may be twisted through an angle of φ, the projected displacement between oxygen ligands. While in principle $0 < \varphi < 60°$, for real apatites twist angles have not been observed to exceed 27°.

While the crystal structures of this family are well defined, eco-apatites are usually formed under conditions far from equilibrium and little detailed crystallographic data is available for such materials. To address this issue we have used X-ray powder diffraction (XRD) and high-resolution transmission electron microscopy (HRTEM) to compare the crystallography of idealized wasteform vanadinites $(Pb_xCa_{10-x})(VO_4)_6F_{2\delta}$, $0 < x < 9$, synthesized using short and long annealing times, to investigate the evolution of Pb/Ca-site partitioning over the A^I and A^{II} positions. In the following paper (Dong & White, 2004) the changes in the A^IO_6 metaprism twist angle (φ) of equilibrated powders are systematized as a function of composition.

2. Experimental methods

Fluoro-vanadinites were synthesized by the solid-state reaction of freshly prepared CaO (obtained by decomposition of AR-grade $CaCO_3$ at 1127 K), PbO, V_2O_5 and CaF_2. The powders were mixed in stoichiometric proportions and fired at 1073 K in alumina boats at ambient atmosphere for 10 h. This firing temperature is just below the melting point of the lead endmember $Pb_{10}(VO_4)_6F_2$. Ten compositions of ideal stoichiometry $(Pb_xCa_{10-x})(VO_4)_6F_2$, $0 < x < 9$, were prepared. In the single case of $(Pb_5Ca_5)(VO_4)_6F_2$, the annealing time was extended to 1, 2 and 7 weeks and samples retained at these intervals. During longer sintering no attempt was made to control fluorine loss through closed-system firing or fluorite overpacking, and $2F^- \leftrightarrow O^{2-}$ substitution was confirmed by semi-quantitative energy-dispersive X-ray analysis (EDX) and subsequent structure refinement.

Powder X-ray diffraction (XRD) patterns were collected using a Siemens D5005 X-ray diffractometer fitted with a Cu-tube operated at 40 kV and 40 mA. Divergence, anti-scatter, receiving and detector slits of

0.5, 0.5°, 0.1 and 0.6 mm, respectively, were inserted. Soller slits in the incident and diffracted paths were used to limit the beam divergence to within 2.3°, and a post specimen monochromator was used to reduce background. Scans were collected from samples rotating around the holder axis at 30 r.p.m. over the angles 10–140° 2θ with a step size of 0.01° and counting time of 5 s per step. Under these conditions the gross intensity of the strongest peak was 2000–3000 counts. Prior to data collection, the fired agglomerates were mechanically ground to fine powders to minimize crystal size effects and mixed with approximately 25 wt.% of standard silicon powder with a_0 = 5.43088 Å (*NIST* 640*c*) to internally calibrate the zero shift.

The crystal structure of $(Pb_5Ca_5)(VO_4)_6(F_{1-2y}O_y)_2$ was refined by Rietveld analysis using the fundamental parameter method as implemented in *TOPAS* (Cheary & Coehlo, 1992, 1998). In the absence of crystallographic data for $Pb_{10}(VO_4)_6F_2$ or $Ca_{10}(VO_4)_6F_2$, the starting model for refinement used the atomic positions for $Ca_{10}(PO_4)_6F_2$ (Sudarsanan *et al.*, 1972) with Ca/Pb occupancy set according to the bulk composition and equal partitioning over the *A* sites. The symmetry $P6_3/m$ was used for all compositions. $Ca_{10}(VO_4)_6F_2$ is strictly monoclinic (Kreidler & Hummel, 1970) and this compound was also refined in $P2_1/m$ (Dong & White, 2004). For each data set, a four-coefficient background polynomial, a zero error and a sample displacement were refined sequentially followed by unit-cell parameters, scale factor and peak shape. Isotropic temperature factors for calcium, lead and vanadium were refined, however, those for oxygen and fluorine were set at 1 Å^2. X-ray scattering factors for the charged species Ca^{2+}, Pb^{2+}, V^{5+}, O^{2-} and F^- were used. Cation positions were refined first, followed by the oxygen positions. To ensure reasonable bond lengths in the VO_4 tetrahedra, fractional coordinates were constrained close to the V—O bond length of 1.735 Å (Shannon & Prewitt, 1970) using a penalty function. Calcium and lead occupancies were then released such that N(Ca) + N(Pb) = 1 was satisfied for the $A^{\rm I}$

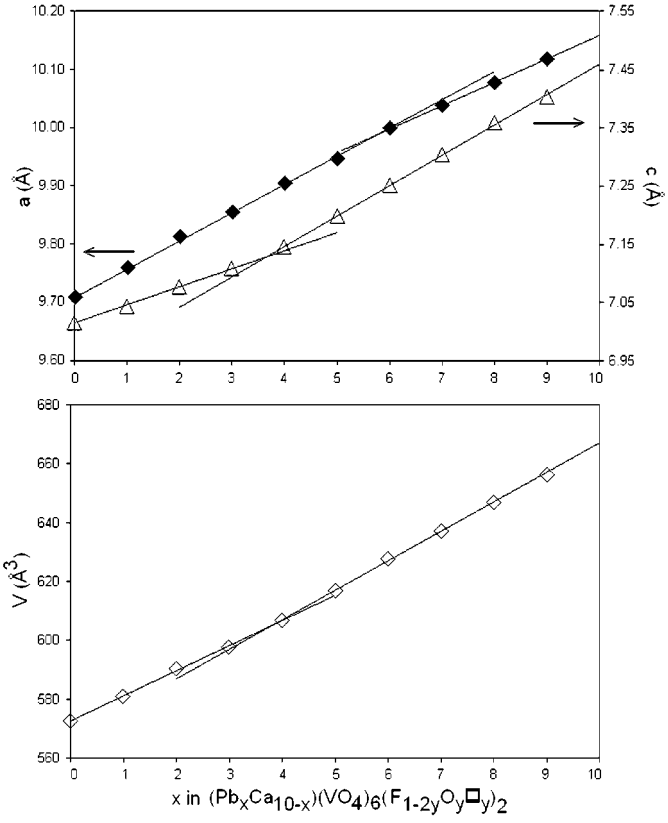

Figure 2
Unit-cell parameter trends after annealing for 10 h at 1073 K for $(Pb_xCa_{10-x})(VO_4)_6(F_{1-2y}O_y\square_y)_2$. Vergard's Law is obeyed in independent compositional segments for *a* and *c*. Error bars are smaller than the graphing symbols (see Table 1).

Table 2
Refined crystal and atomic parameters for vanadinite of idealized stoichiometry $(Pb_xCa_{10-x})(VO_4)_6(F_{1-2y}O_y\square_y)_2$ annealed at 1073 K for intervals from 10 h to 7 weeks.

10 h: $(Pb_{4.62}Ca_{5.38})(VO_4)_6F_2 \simeq [Pb_{1.56}Ca_{2.44}][Pb_{2.06}Ca_{2.94}](VO_4)_6F_2$;
1 week: $(Pb_{4.90}Ca_{5.10})(VO_4)_6(F_{0.6}O_{0.7}) \simeq [Pb_{1.12}Ca_{2.88}][Pb_{3.78}Ca_{2.22}](VO_4)_6(F_{0.6}O_{0.7})$;
2 weeks: $(Pb_{4.78}Ca_{5.22})(VO_4)_6(F_{0.6}O_{0.7}) \simeq [Pb_{0.64}Ca_{3.36}][Pb_{4.14}Ca_{1.96}](VO_4)_6(F_{0.5}O_{0.75})$;
7 weeks: $(Pb_{4.76}Ca_{5.64})(VO_4)_6(F_{0.6}O_{0.7}) \simeq [Pb_{0.68}Ca_{3.32}][Pb_{4.08}Ca_{1.92}](VO_4)_6(F_{0.6}O_{0.7})$.

Annealing time	10 h	1 week	2 weeks	7 weeks
R_{wp}†	0.176	0.180	0.183	0.190
S_{wp}	1.1	1.1	1.1	1.2
R_b	0.042	0.044	0.050	0.049
a (Å)	9.9462 (1)	10.0011 (1)	10.0025 (2)	10.0124 (2)
c (Å)	7.1983 (1)	7.1993 (1)	7.1858 (1)	7.1880 (1)
V (Å^3)	616.7 (2)	623.6 (1)	622.6 (2)	624.0 (2)
c/*a*	0.7237	0.7199	0.7184	0.7179
N(Ca1) (4*f* position)	0.61 (6)	0.72 (4)	0.84 (4)	0.83 (4)
N(Ca2) (6*h* position)	0.49 (6)	0.37 (6)	0.31 (7)	0.32 (7)
$k_{Pb}(A^{\rm I}/A^{\rm II})$	0.52	0.30	0.16	0.17
z(*A*1)	0.0095 (8)	0.0083 (8)	0.0062 (11)	0.0059 (12)
B(*A*1)	0.6	1.2	0.4	1.4
x(*A*2)	0.2427 (3)	0.2442 (2)	0.2418 (2)	0.2426 (2)
y(*A*2)	0.0023 (4)	0.0028 (3)	0.0026 (3)	0.0036 (3)
B(*A*2)	0.6	1.1	1.3	1.7
x (V)	0.4020 (7)	0.4066 (5)	0.4090 (6)	0.4093 (6)
y(V)	0.3758 (6)	0.3770 (5)	0.3813 (6)	0.3805 (6)
B(V)	0.3	0.2	0.2	0.6
x(O1)	0.3195 (18)	0.3363 (16)	0.3407 (17)	0.3393 (18)
y(O1)	0.4915 (18)	0.5014 (16)	0.5073 (16)	0.5057 (17)
x(O2)	0.6012 (20)	0.6046 (19)	0.6056 (20)	0.6074 (20)
y(O2)	0.4755 (18)	0.4782 (16)	0.4787 (17)	0.4807 (17)
x(O3)	0.3353 (13)	0.3436 (10)	0.3545 (10)	0.3499 (11)
y(O3)	0.2546 (13)	0.2594 (11)	0.2635 (11)	0.2639 (12)
z(O3)	0.0628 (13)	0.0602 (13)	0.0605 (13)	0.0583 (14)
N(F)	1.0 (3)	0.6 (2)	0.5 (2)	0.6 (2)
φ (°)	22.0	16.1	14.5	14.4

† Agreement measures are $R_{wp} = [(\sum_i w_i|y_{io} - y_{ci}|^2)/\sum_i w_i y_{io}^2]^{1/2}$, $S_{wp} = (R_{wp}/R_{exp})^2$ and $R_b = \sum_i |I_{ko} - I_{kc}|/\sum_i I_{ko}$.

Table 3
Selected bond distances (Å) in (Pb $_x$Ca$_{10-x}$)(VO$_4$)$_6$(F$_{1-2y}$O$_{yy}$)$_2$ as a function of sintering time.

	10 h	1 week	2 weeks	7 weeks
$A^{\rm I}$—O1 × 3	2.409 (14)	2.410 (15)	2.394 (14)	2.403 (14)
$A^{\rm I}$—O2 × 3	2.612 (20)	2.616 (18)	2.601 (19)	2.605 (19)
Average	**2.511**	**2.513**	**2.498**	**2.504**
$A^{\rm II}$—O1	2.913 (14)	3.073 (16)	3.126 (15)	3.122 (14)
$A^{\rm II}$—O2	2.434 (18)	2.409 (16)	2.426 (15)	2.404 (16)
$A^{\rm II}$—O3 × 2	2.578 (13)	2.622 (12)	2.645 (12)	2.654 (12)
$A^{\rm II}$—O3 × 2	2.418 (11)	2.440 (11)	2.471 (11)	2.440 (11)
$A^{\rm II}$—F/O	2.403 (3)	2.428 (3)	2.406 (3)	2.411 (3)
Average	**2.535**	**2.576**	**2.598**	**2.589**
V—O1	1.715 (23)	1.708 (24)	1.708 (22)	1.715 (22)
V—O2	1.716 (22)	1.715 (21)	1.703 (22)	1.718 (21)
V—O3 × 2	1.704 (11)	1.704 (10)	1.702 (11)	1.709 (11)
Average	**1.710**	**1.708**	**1.704**	**1.713**

and $A^{\rm II}$ cations – less than 100% occupancy was not considered. Patterns were analysed systematically from the calcium to lead end-members. In all refinements the apatite was treated as a single phase, although for $Ca_{10}(VO_4)_6F_2$ a trace of $Ca_3(VO_4)_2$ was present.

For high-resolution transmission electron microscopy (HRTEM) powdered specimens were dispersed with ethanol in an ultrasonic bath for 5 min and a drop of suspension deposited onto a holey carbon-coated copper grid. Images were collected digitally using a JEM-3010 microscope (C_s = 1.2 mm) operated at 300 kV and fitted with a low-background Gatan double tilt holder. Crystals were tilted to $\langle 2\bar{1}\bar{1}0\rangle$ and [0001] zone axes. Simulated images were calculated by the multislice method (Stadelmann, 1987) using as a starting point the average structures determined by XRD refinement. A slice thickness of about 3 Å was used and the absorption coefficient fixed as 0.1. Other parameters included in the simulation process were objective aperture diameter $\simeq$ 10 nm^{-1}, spread of focus ~10 nm and beam semi-convergence

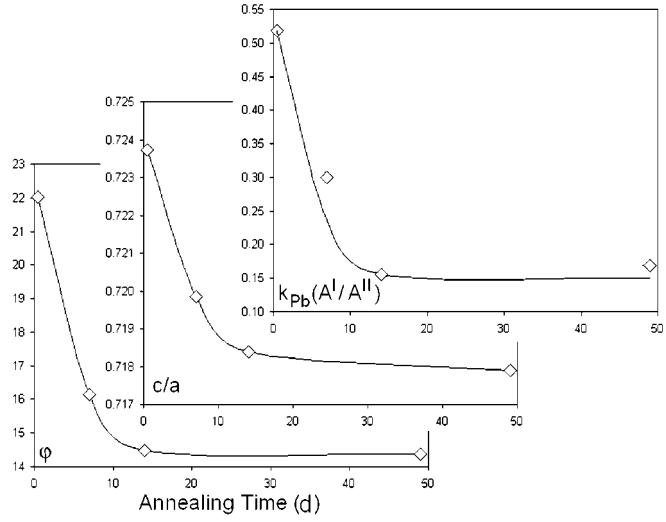

Figure 3
Correlations in $k_{\rm Pb}(A^{\rm I}/A^{\rm II})$, c/a and φ in $(Pb_5Ca_5)(VO_4)_6F_2$ as a function of annealing time.

Table 4
Symmetry of apatite-family members.

	Special projections	
Space group	[001]	[100]
$P6_3/m$ (176)	$p6$	$p2g\ m$
$P\bar{6}$ (174)	$p3$	$p11m$
$P6_3$ (173)	$p6$	$p1g\ 1$
$P\bar{3}$ (147)	$p6$	$p2$
$P2_1/m$ (11)	$p2$	$p2g\ m$

~0.8 mrad. Digital filtering and tests for local symmetry were carried out using Fourier filtering methods, as implemented in *CRISP* (Hovmöller, 1992).

3. Results

3.1. Variations with composition

The unit-cell constants and *A*-site partitioning coefficients for the vanadinites annealed for 10 h are collected in Table 1. As $(Pb_xCa_{10-x})(VO_4)_6F_2$ became progressively more plumbous the lattice parameters dilate as the lead (effective ionic radii = 1.29 Å for VIII coordination) to calcium (1.12 Å) ratio increases (Shannon & Prewitt, 1970) (Fig. 2). Dilation of the *a* and *c* edges did not obey Vergard's law over the entire compositional join, but were composed of two linear segments such that

$$a = 9.7073 + 0.04693x \quad \text{for} \quad 0 < x < \sim 6 \qquad (1a)$$

$$a = 10.1579 - 0.04036(1 - x) \quad \text{for} \quad \sim 7 < x < 10 \qquad (1b)$$

$$c = 7.0153 + 0.03091x \quad \text{for} \quad 0 < x < \sim 3 \qquad (2a)$$

$$c = 7.4585 - 0.05205(1 - x) \quad \text{for} \quad \sim 4 < x < 10 \qquad (2b)$$

$$\text{Volume} = 572.5 + 8.5282x \quad \text{for} \quad 0 < x < \sim 3 \qquad (3a)$$

$$\text{Volume} = 667.05 - 10.045(1 - x) \quad \text{for} \quad \sim 4 < x < 10. \qquad (3b)$$

In all cases the fit residuals $R^2 > 0.99$. The rate of change of the lattice parameters as a function of composition is controlled by the partitioning of lead and calcium, which in turn determines the rate of change of the metaprism twist angle (φ) (Dong & White, 2004). As described below, the materials annealed for 10 h had not attained equilibrium, the partitioning coefficient for lead over the $A^{\rm I}$ and $A^{\rm II}$ sites did not vary systematically (Table 1), and HRTEM revealed substantial disorder at the unit-cell scale. While structure refinement from such powders represents an averaging of local structures, for all compositions $k_{\rm Pb}$ was less than the expected value for equal partitioning over the large cation sites, indicating lead enrichment of the $A^{\rm II}$ position (Table 1). It should be noted that the correlations between cell constants and composition for these vanadinates in disequilibrium are quite distinct from those obtained for equilibrated material (see Fig. 2 in Dong & White, 2004).

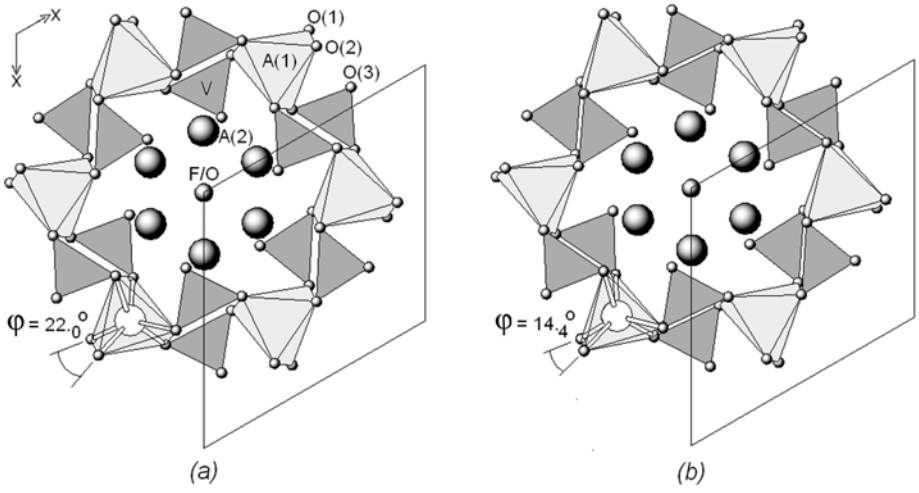

Figure 4
Polyhedral representations of (*a*) the 'average structure' of non-equilibrated $(Pb_{4.62}Ca_{5.38})(VO_4)_6F_2 \simeq [Pb_{1.56}Ca_{2.44}][Pb_{2.06}Ca_{2.94}](VO_4)_6F_2$ and (*b*) the equilibrated structure of $(Pb_{4.76}Ca_{5.64})(VO_4)_6(F_{0.6}O_{0.7}) \simeq [Pb_{0.68}Ca_{3.32}][Pb_{4.08}Ca_{1.92}](VO_4)_6(F_{0.6}O_{0.7})$ projected down [0001]. The A^IO_6 metaprisms and VO_4 tetrahedra are emphasized to highlight the cooperative movements of these polyhedra. Not shown are three more distant O atoms that cap each (0001) metaprism face.

3.2. Variations with annealing time

Annealing of $Pb_5Ca_5(VO_4)_6F_{2\delta}$ at 1073 K for a cumulative total of 7 weeks resulted in a reduction in the *c*/*a* ratio that advanced especially rapidly in the first 2 weeks (Fig. 3*b*), beyond which the cell parameters stabilized (Table 2). Relatively small changes from 2–7 weeks firing are most probably related to incipient vanadium reduction and/or loss of fluorine and lead. The trend in the axial ratio was tracked by k_{Pb} and the metaprism twist angle φ. A significant redistribution of lead occurred with the A^{II} site becoming substantially enriched (Fig. 3*c*). After 7 weeks $k_{Pb}(A^I/A^{II})$ was 0.17 compared with 0.52 for 10 h material. As the A^IO_6 metaprism lost lead, the apatite channel expanded to accommodate

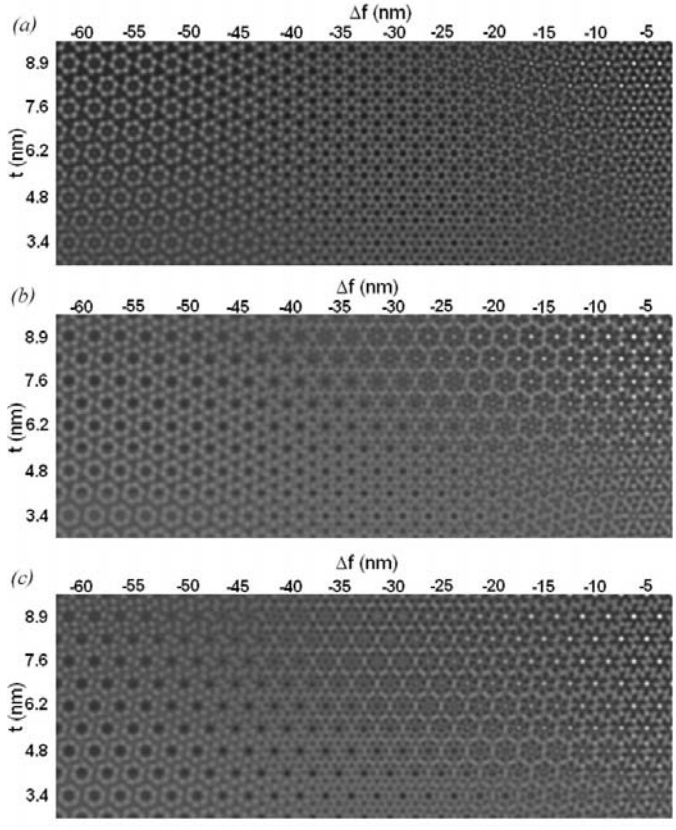

Figure 5
Calculated [0001] high-resolution electron microscope images for $(Pb_xCa_{10-x})(VO_4)_6(F)_2$ with (*a*) $x = 0$, (*b*) $x = 5$ and (*c*) $x = 10$. Input crystal and atomic parameters were derived from refined X-ray diffraction data. Substantial contrast differences appear over the compositional range that can be recognized in experimental images.

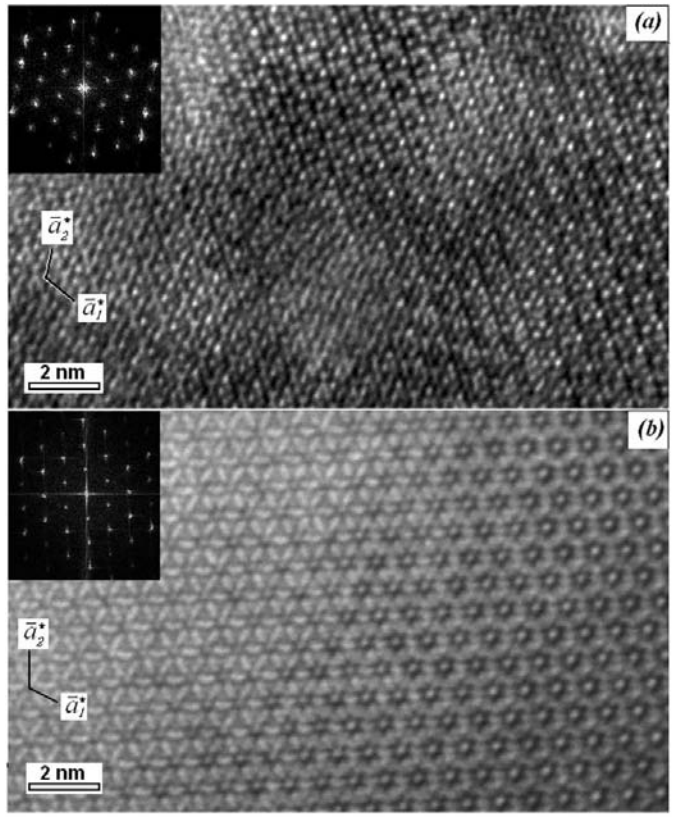

Figure 6
[0001] high-resolution electron micrographs collected from $(Pb_5Ca_5)(VO_4)_6(F_{1-2y}O_y)_2$ thin crystal wedges annealed for (*a*) 10 h and (*b*) 7 weeks. Inserts of the power transforms confirm the orientation. The upper image is poorly equilibrated with microdomains 2 nm in diameter arising from local variation in Ca/Pb content, as would be anticipated from the multislice simulations (see Fig. 5). Conversely, the equilibrated sample shows regular contrast changes in passing from the thin edge (left) to the thicker crystal (right).

additional lead with φ becoming more acute and ultimately reducing to $14._4^\circ$ from $22._0^\circ$ (Fig. 3*a*).

Throughout annealing the VO_4 tetrahedra were essentially invariant with an average V—O bond length of 1.71 Å, a figure somewhat smaller than the soft constraint value of 1.735 Å. The $A^{\rm I}O_6$ metaprism bonds contracted slightly and the $A^{\rm II}O_6F$ polyhedron expanded as Pb/Ca partitioning was established (Table 3). The disposition of the $A^{\rm I}O_6$ and VO_4 polyhedra before and after annealing is illustrated in Fig. 4. In disequilibrium the metaprisms are substantially twisted, as the channels are rich in smaller calcium, which in turn drives apart the regular VO_4 tetrahedra. The refinements also suggest that some fluorine loss occurred, probably through replacement of $2F^- \rightarrow O^{2-}$, but this could not be examined in detail using the current data.

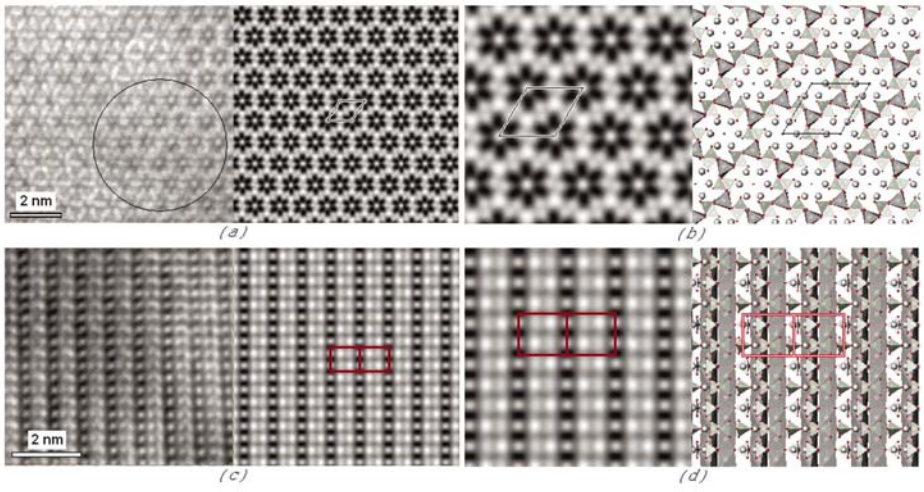

Figure 7
(*a*) High-resolution [0001] experimental image of equilibrated $(Pb_5Ca_5)(VO_4)_6(F_{1-2y}O_y)_2$ before and after Fourier processing and the imposition of *p*6 symmetry. The Fourier envelope was prepared from the region within the circle. (*b*) Enlarged portion of the processed image and the correspondence to the apatite structure as determined by Rietveld refinement. (*c*) High-resolution $[2\bar{1}\bar{1}0]$ experimental image of non-equilibrated $(Pb_3Ca_7)(VO_4)_6(F_{1-2y}O_y)_2$ before and after Fourier processing and the imposition of *p*2*gm* symmetry. The Fourier envelope was prepared from the total area displayed in the raw image. (*d*) Enlarged portion of the processed image and the correspondence to the apatite structure as determined by Rietveld refinement.

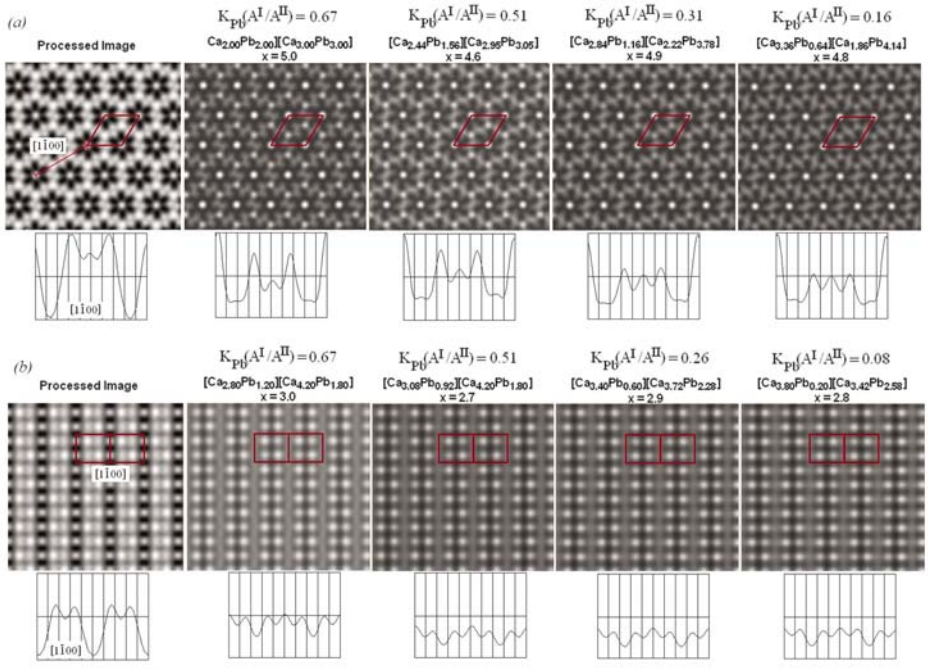

Figure 8
Multislice matching (right-hand images) compared with processed images (on the left) for (*a*) the [0001] projection of equilibrated $(Pb_5Ca_5)(VO_4)_6(F_{1-2y}O_y)_2$ using a range of $k_{Pb}(A^I/A^{II})$ with $\Delta f = -10$ nm and $t = 8.3$ nm. Contrast line traces along $[1\bar{1}00]$ show reasonable qualitative matching, but the k_{Pb} models could not be assigned absolutely, and (*b*) the $[11\bar{2}0]$ projection of non-equilibrated $(Pb_3Ca_7)(VO_4)_6(F_{1-2y}O_y)_2$ using a range of $k_{Pb}(A^I/A^{II})$, $\Delta f = -32$ nm and $t = 4.7$ nm. Agreement between the processed and calculated images, as exemplified by the contrast line trace along $[1\bar{1}00]$, was poorer and in the processed image there appears to be axial doubling vertically along [0001].

3.3. $A^{\rm I}/A^{\rm II}$ local disorder

The investigation of cation order–disorder in apatites by HRTEM is challenging on two counts. First, it is well known that for some compositions (especially the extensively studied hydroxyapatite *HAp*), etching and amorphization can proceed rapidly unless low electron fluxes and/or cooled specimen stages are used (*e.g.* Sato *et al.*, 2002). However in a supplementary investigation, Dong *et al.* (2004) established that while vanadinite will undergo an electron-beam-induced transformation to perovskite *via* glaserite when subjected to intense or prolonged irradiation, the conditions used in the current experiments were relatively mild and would not have compromised the structure beyond partial loss of fluorine. Second, the structure of apatite is relatively complex and without the benefit of a short (~ 3 Å) crystallographic projection providing an unobscured view of homoatomic cation columns, intuitive interpretation of HRTEM images is impossible. For the specific case of lead substitution in *HAp*, calculations by Brès *et al.* (1986) suggested that microchemical ordering over the $A^{\rm I}$ and $A^{\rm II}$ sites may be recognized in thicker crystals when viewed along $[2\bar{1}\bar{1}0]$ with a 400 keV microscope. Our calculations of [0001] thickness defocus wedges for $(Ca_{10})(VO_4)_6F_2$, $(Pb_5Ca_5)(VO_4)_6F_2$ and $(Pb_{10})(VO_4)_6F_2$ also imply that unit-cell scale fluctuations in Ca/Pb

ratio will be detectable as subtle changes in image contrast (Fig. 5). Basal plane micrographs collected from short-annealed non-equilibrated material displayed obviously mottled contrast ascribed to short-range compositional disorder (Fig. 6*a*). However, longer heat treatment yielded crystals with a regular progression of contrast from thinner to thicker regions (Fig. 6*b*).

3.4. Image processing

The subgroups adopted by apatites are summarized in Table 4 along with the plane symmetries for the [100] $\equiv$ [$2\bar{1}\bar{1}0$] and [001] $\equiv$ [0001] special projections (White & Dong, 2003). Using the methods of Hovmöller (1992) and Zou *et al.* (1996), Fourier processing of equilibrated $(Pb_5Ca_5)(VO_4)_6(F_{2-2y}O_y)_2$ [0001] images yielded comparable figures of merit ($R_{\rm amplitudes}$ and $\varphi_{\rm res}$) for *p* 6 (consistent with space groups $P6_3/m$, $P6_3$, $P\bar{3}$, $P2_1/m$) and *p* 3 ($P\bar{6}$) symmetries (Fig. 7*a*). A similar analysis of non-equilibrated $(Pb_3Ca_7)(VO_4)_6(F_{1-2y}O_y)_2$ [$2\bar{1}\bar{1}0$] images consistently gave equivalent results for *p* 1*g* 1 and p 2*g m* (Fig. 7*c*). Therefore, either $P6_3/m$ or $P6_3$ are possible space groups for these apatites. Following normal crystallographic practice, the former symmetry high space group is considered correct and is consistent with Rietveld analyses that show no improvement in *R* factors when a $P6_3$ refinement model was used. The correspondence of the potential maps to the crystal structures are illustrated in Figs. 6(*b*) and (*d*).

Simulated [0001] and [$2\bar{1}\bar{1}0$] images of $(Pb_5Ca_5)(VO_4)_6(F_{1-2y}O_y)_2$ and $(Pb_3Ca_7)(VO_4)_6(F_{1-2y}O_y)_2$ were calculated from input data derived from Rietveld refinement. For equilibrated [0001] the relative intensities of the processed and simulated images agree well (Fig. 8*a*). For $x = 0.5$ and with $0.16 < k_{\rm Pb} < 0.67$, the images are relatively insensitive to the $k_{\rm Pb}$ used and the potential maps cannot differentiate *A*-cation ordering quantitatively. On the other hand, for non-equilibrated samples the [$11\bar{2}0$] of calculated and experimental intensities were quite dissimilar, although an extensive exercise in varying crystallographic and microscope parameters was undertaken to obtain a more satisfactory match.

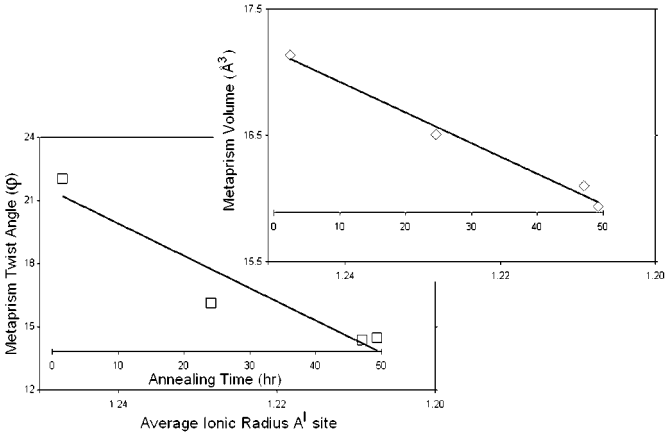

Figure 9
The dependence of φ and metaprism volume as a function of the average ionic radius of $A^{\rm I}$.

4. Discussion

The *a* and *c* cell constants varied linearly in compliance with Vergard's Law over two compositional ranges $0 < x < \sim 3.5$ and $\sim 3.5 < x < 10$ (Fig. 2). This behaviour suggests that while the materials were single phase over the entire compositional range, long annealing of compositions close to $(Pb_{3.5}Ca_{6.5})(VO_4)_6(F_{1-2y}O_y)_2$ may promote phase separation, which was subsequently confirmed (Dong & White, 2004). A reduction in slope of the cell parameters as a function of composition indicates that the rate of change of φ has changed due to different modes of channel filling. There was no correlation of $k_{\rm Pb}$ with lattice constants, as unit-cell scale disorder was 'averaged' during refinement in a manner not accommodated by the Rietveld model.

During long-term annealing, metaprism volume and φ decreased linearly as a function of the average $A^{\rm I}$ ionic radius (Fig. 9). For $(Pb_5Ca_5)(VO_4)_6(F_{1-2y}O_y)_2$ vanadinite annealed from 10 h to 7 weeks, φ ranged from $22._0$ to $14._4{}^\circ$ such that the $A^{\rm I}-$O bond lengths decreased slightly, with simultaneous lead enrichment of $A^{\rm II}$ leading to expansion of the tunnel cavity and an increase in the average bond length of the $A^{\rm II}O_6F$ polyhedra from 2.535 to 2.589 Å. Tunnel opening is accomplished through reduction in φ, although the precise significance of the twist angles refined from the short annealed and heavily disordered vanadinite is not certain.

The kinetics for attaining equilibrium are quite slow and several weeks annealing near the melting point are required to stabilize $k_{\rm Pb}$ with disequilibrium yielding HRTEM images interpretable as microdomains of variable Ca/Pb content. Longer firing serves to steady partitioning, but vanadium reduction and/or loss of lead and fluorine may become significant over extended periods. While most compositions could be satisfactorily fitted to $P6_3/m$ [the exception being $P2_1/m$ $Ca_{10}(VO_4)_6F_2$], the presence of local regions with lower symmetry in the poorly equilibrated vanadinite should not be ruled out, despite reasonable matching of the Fourier processed images with simulated images. In these materials the inability to match semi-quantitatively the contrast in [$2\bar{1}\bar{1}0$] processed images and simulations is consistent with differences of $k_{\rm Pb}$ at the unit-cell level. Careful inspection of the [$11\bar{2}0$] processed image (Fig. 8*b*) shows that at short range the unit cell may be doubled along [0001].

The authors would like to thank Ms Wei Bing for her help in apatite powder sintering. This work was supported through A*STAR Grant 012 105 0123.

References

Brès, E. F., Voegel, J. C., Barry, J. C., Waddington, W. G. & Frank, R. M. (1986). *J. Appl. Cryst.* **19**, 168–173.
Calos, N. J. & Kennard, C. H. L. (1990). *Z. Kristallogr.* **191**, 125–129.
Carrillo-Cabrera, W. & von Schnering, H. G. (1999). *Z. Anorg. Allg. Chem.* **625**, 183–185.

Cheary, R. W. & Coelho, A. A. (1992). *J. Appl. Cryst.* **25**, 109–121.
Cheary, R. W. & Coelho, A. A. (1998). *J. Appl. Cryst.* **31**, 851–861.
Dai, Y.-S. & Hughes, J. M. (1989). *Can. Mineral.* **27**, 189–192.
Dong, Z. L., Sun, K., Wang, L. M., White, T. J. & Ewing, R. C. (2004). *J. Am. Ceram. Soc.* In the press.
Dong, Z. L. & White, T. J. (2004). *Acta Cryst.* B**60**, 146–154.
Elliott, J. C. (1973). *Clin. Orthopaed. Rel. Res.* **93**, 313–345.
Habelitz, S., Pascual, L. & Durán, A. (1999). *J. Eur. Ceram. Soc.* **19**, 2685–2694.
Hovmöller, S. (1992). *Ultramicroscopy*, **41**, 121–135.
Ioannidis, T. A. & Zouboulis, A. I. (2003). *J. Hazard. Mater. B*, **97**, 173–191.
Ito, A., Akao, M., Miura, N., Otsuka, R. & Tsutsumi, S. (1988). *Nippon Seramikkusu Kyokai Gakujutsu Ronbunshi*, Vol. 96, pp. 305–309. (Abstracted from ICSD, Collection Code 68336, Gmelion Institute, Fiz Karlsruhe).
Jeanjean, J., Vincent, U. & Fedoroff, M. (1994). *J. Solid State Chem.* **108**, 68–72.
Kim, J. Y., Fenton, R. R., Hunter, B. A. & Kennedy, B. J. (2000). *Aust. J. Chem.* **53**, 679–686.
Kreidler, E. R. & Hummel, F. A. (1970). *Am. Mineral.* **55**, 170–184.
Sato, K., Kogure, T., Iwai, H. & Tanaka, J. (2002). *J. Am. Ceram. Soc.* **85**, 3054–3058.
Shannon, R. D. & Prewitt, C. T. (1970). *Acta Cryst.* B**26**, 1046–1048.
Stadelmann, P. A. (1987). *Ultramicroscopy*, **21**, 131–146.
Sudarsanan, K., Mackie, P. E. & Young, R. A. (1972). *Mater. Res. Bull.* **7**, 1331–1338.
White, T. J. & Dong, Z. L. (2003). *Acta Cryst.* B**59**, 1–16.
White, T. J., Dong, Z. L. & Kim, J. (2004). *Mater. Trans.* In the press.
Zhang, P. & Ryan, J. A. (1999). *Environ. Sci. Technol.* **33**, 625–630.
Zou, X., Sunberg, M., Larine, M. & Hovmöller, S. (1996). *Ultramicroscopy*, **62**, 103–121.